Anisotropic Growth Control of Polyaniline Nanostructures and Their Morphology-Dependent Electrochemical Characteristics

Hyun-Woo Park, Taejoon Kim, Jinyoung Huh, Minjeong Kang, Ji Eun Lee, and Hyeonseok Yoon*

Alan G. MacDiarmid Energy Research Institute, Department of Polymer and Fiber System Engineering, Chonnam National University, Gwangju 500-757, South Korea

ABSTRACT Polyaniline (PANI) is one of the most widely investigated conducting polymers and is considered to be of practical use for many future applications.

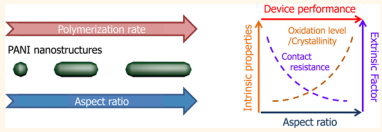

Here, we first demonstrate that the anisotropic growth of PANI at the nanometer scale can be kinetically controlled by employing a polymeric stabilizer, poly(*N*-vinylpyrrolidone). The polymerization rate became slower in the presence of the stabilizer (the rate constants calculated at the initial stage decreased with increasing concentration of the stabilizer), yielding PANI nanostructures with lower aspect ratios. Therefore, it is believed that the stabilizer sterically restricts the directional fiber growth mechanism governing PANI chain growth in aqueous solution. Three PANI nanostructures, specifically nanospheres, nanorods, and nanofibers, were fabricated and their oxidation/protonation levels were investigated systematically. It was found that the nanofibers had the most outstanding oxidation/protonation level accompanied by structural ordering (note that the only difference between the polymerization conditions in each case was the concentration of the stabilizer). We also examine the electrochemical properties of PANI nanostructure electrodes in three-electrode and two-electrode (actual capacitor cell) configurations. The intrinsic charge-transport ability of individual nanostructures strongly affected the electrochemical properties of the electrodes. Briefly, the nanofiber electrode had faster electrode kinetics and better capacitance than the nanorods and nanospheres. Lastly, an extrinsic factor, the interparticle contact resistance, also turned out to noticeably influence the capacitances of the electrodes.

KEYWORDS: polyaniline · conducting polymers · nanostructures · morphology control · electrochemical properties

In recent years, there has been burgeoning interest in the synthesis and application of conducting polymers.[1,2] By virtue of their fascinating physical and chemical properties, conducting polymers have demonstrated a wide range of applications in the main areas of electronics, optics, and energy conversion/storage.[3−7] In particular, nanostructured conducting polymers have offered unique opportunities for creating innovative applications in the aforementioned areas,[8−14] which mainly result from their beneficial characteristics at the nanometer scale. The most striking characteristic is that the properties of these materials become dependent on their size and shape when their dimensions are decreased to the nanoscale. To investigate the size− or shape−property relationship in nanomaterials, above all, it is necessary to develop reliable synthetic methods that can precisely tailor the nanomaterials. Much effort has so far been devoted to designing and synthesizing various kinds of nanomaterials. Compared to inorganic nanomaterials, however, it is intrinsically difficult to control the morphology of organic polymer nanomaterials whose dimensional stability drops dramatically at the nanoscale.[15]

Polyaniline (PANI) is one of the most useful conducting polymers due to its good electrical properties and environmental stability.[16,17] Notably, the Kaner group exploited a facile synthetic strategy for generating PANI nanofibers without the use of any templates,[18] which spurred extensive study on PANI nanofibers.[19−24] The nanofibrillar structure offers excellent opportunities for studying one-dimensional systems at the nanometer scale.[25,26] Accordingly, many research groups have reported the utilization of PANI nanofibers as key building blocks for fabricating functional nanocomposites,[27−30] chemical sensors,[31−34] nonvolatile memories,[35,36] catalytic supports,[37] supercapacitors,[38−40] and batteries.[41] It appears that the inherent anisotropic geometry of PANI nanostructures provides significant advantages over their bulky counterparts. However, there is limited information available on what factors lead to better performance in the above applications.

Here we synthesize PANI nanostructures of three different shapes of which the aspect ratios are controlled, namely, nanospheres,

* Address correspondence to hyoon@chonnam.ac.kr.

Received for review December 16, 2011 and accepted August 18, 2012.

Published online August 19, 2012
10.1021/nn3033425

nanorods, and nanofibers. A polymeric stabilizer is employed to provide a steric effect in the PANI chain growth which allows tailoring of the morphology of the resulting PANI nanostructures. The three nanostructures were generated under the same polymerization conditions except for the concentration of the stabilizer, and thus they present a good model system for studying the structure–property relationship of the conducting polymer in the nanometer regime. A distinguishing feature of conducting polymers is their electrical characteristics, which are similar to those of metals or inorganic semiconductors. Therefore, we explore what factors determine the device performance when PANI nanostructures are used as the electrode-active materials for the model device, a supercapacitor.

RESULTS AND DISCUSSION

PANI nanofibrillar structures have been generated with the aid of specific structure-directing agents such as surfactants, large organic dopants, polyelectrolytes, nanowire seeds, and oligomers.[19−24] These studies have demonstrated that PANI tends to intrinsically form into a nanofibrillar morphology in polar environments. In this work, PANI nanostructures were chemically synthesized in acidic aqueous solution *via* a kind of dispersion polymerization where the monomer aniline is soluble and the resulting polymer is insoluble. The nanofibrillar structures, namely, nanofibers, were readily obtained without the use of any structure-directing agents, as reported previously. In the presence of a steric stabilizer, poly(*N*-vinylpyrrolidone) (PVP), however, the morphology of the resulting polymer could be tuned instead to nanospheres or nanorods, depending on the concentration of PVP. Figure 1 exhibits scanning electron microscopy (SEM) images of three PANI nanostructures synthesized with different PVP concentrations at the same stirring condition. The diameters of the nanostructures were similarly found to be around 50 nm, and the lengths of the nanorods and nanofibers were about 150 and 215 nm, respectively (see the histogram).

From a mechanistic point of view, chemical oxidation polymerization of aniline with ammonium persulfate produces small oligomeric intermediates such as dimers and trimers in the beginning of the reaction. The oligomers continue to grow through reacting with each other or with monomers. During this process, the interfacial tension between the growing oligomer chain and the reaction medium significantly affects the morphology of the resulting polymer. While aniline is soluble in aqueous solution, PANI is insoluble. Thus, it can be easily expected that the interfacial tension of the growing oligomer chain in the aqueous medium becomes high with increasing chain length. The second main factor determining the morphology of the resulting polymer is the polymerization kinetics. When the polymerization proceeds slowly, long-chain oligomers with relatively low solubility (*i.e.*, high interfacial tension) can coagulate into globular shapes in the medium, which in turn results in the formation of spherical particles. On the other hand, a rapid polymerization rate may not allow enough time for the long-chain oligomers to coagulate, which may lead to the generation of one-dimensional structures such as fibrils.

Under our experimental conditions, the color of the polymerization medium changed from transparent to blue and then deep green. It is known that PANI has four different oxidation states along with their inherent colors: (a) leucoemeraldine base (fully reduced form with pale yellow color), (b) emeraldine base (half-oxidized form with blue color), (c) emeraldine salt (half-oxidized and protonated form with green color), and (d) pernigraniline base (fully oxidized form with blue/violet color). Importantly, the time when the color appeared to change depended on the synthesis conditions. This fact indicates that the polymerization rate would be different for each synthesis condition. To gain in-depth insight into this observation, the open-circuit potential was monitored during the polymerization. The reaction rate can be affected by stirring condition over the polymerization process. As a notable example, the Kaner group described the effect of extremely different stirring conditions, namely, vigorous stirring *versus* no stirring on the final morphology of PANI nanostructures.[42] In addition, lateral shear force by stirring may influence the morphology evolution of PANI nanostructures. Hence the stirring condition, as well as PVP concentration, was adjusted within a moderate range to examine its effect on the morphology of the resulting PANI nanostructures. Typical plots of open-circuit potential against time are shown in Figure 2. After introducing the oxidizing agent to the monomer/stabilizer solution, the polymerization proceeded *via* the following stages: (i) a short induction period, (ii) the appearance of a blue color in the polymerization medium, and (iii) a change of the color to green. These stages were labeled as I, II, and III in the potential-time profile. Briefly, the first stage is a typical induction period for the oxidative polymerization of aniline in acidic media (stage I). Manohar and co-workers reported that colorless anilinium–peroxydisulfate ion aggregates generated during the induction period and their shape determine the overall morphology of the product, PANI emeraldine salt.[20] Pernigraniline chains grow to attain high molecular weights in the second period (stage II), and last the pernigraniline is reduced to the emeraldine salt (stage III). The molecular weight of the resulting polymer is almost determined at the end of stage II. Therefore, the duration of stages I and II reflects the rate of the overall polymerization process.

Under the same PVP concentrations, no remarkable difference was observed in the potential profiles. Therefore, it is considered that the mild stirring conditions of

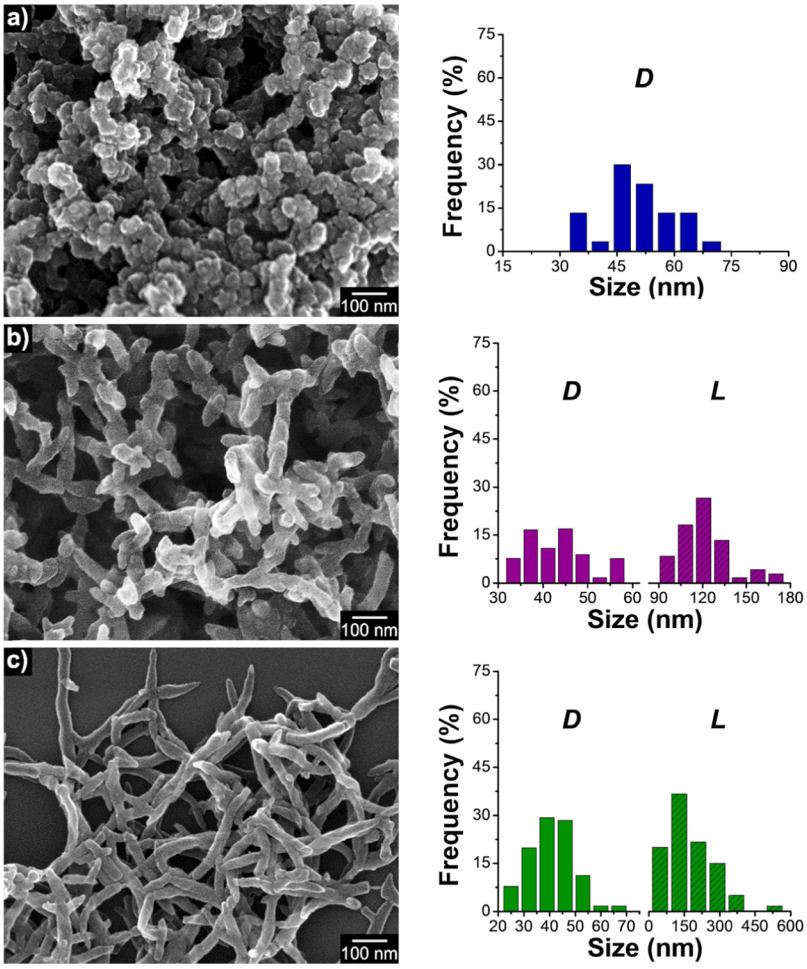

Figure 1. FE-SEM images of PANI nanostructures with different aspect ratios synthesized at the same stirring condition (200 rpm) and histograms showing their size distribution (*D*, diameter; *L*, length): (a) nanospheres, (b) nanorods, and (c) nanofibers.

200−500 rpm had no significant influence on the final morphology of the PANI nanostructures. This result was further confirmed by SEM observation (see Supporting Information). On the other hand, the nanofibers clearly had the shortest duration of stages I and II (131 ± 8 s), followed by the nanorods (169 ± 6 s) and then the nanospheres (197 ± 4 s). That is to say, it turned out that the faster the rate of polymerization, the higher the aspect ratio of the resulting nanostructure.

Further in-depth insight can be given regarding stage I, which may strongly affect the morphology of the final product. At this stage, the following oxidation reaction is expected to be dominant:

$$\text{aniline} + \text{APS} \rightarrow \text{aniline}^{+}$$

where APS is the abbreviation of ammonium persulfate and aniline^{+} represents the oxidized monomer. A simple kinetic equation for the above reaction is proposed as follows:

$$\mathrm{d}[M]/\mathrm{d}t = -k[M][I] \quad (1)$$

where *M*, *I*, and *k* denote the aniline monomer, APS initiator, and rate constant, respectively. If 1 mol of aniline is consumed by 1.25 mol of APS,[43] the concentration of APS is expressed as

$$[I] = [I]_0 - 1.25([M]_0 - [M]) \quad (2)$$

Substituting eq 2 into eq 1 and then integrating it gives

$$[M(t)] = \beta_1[M]_0 e^{\beta_2 t}/\{0.8[I]_0 - [M]_0 e^{\beta_2 t}\} \quad (3)$$

where

$$\beta_1 = 0.8[I]_0 - [M]_0 \text{ and } \beta_2 = -1.25\beta_1 k$$

The time-dependent change in the open-circuit potential ([*E*(*t*)]) is considered to be inversely proportional to the rate of monomer depletion ([*M*(*t*)]) and thus the following correlation can be proposed:

$$[E(t)] = K/[M(t)] \quad (4)$$

Here, *K* is a proportionality factor scaling the change. The important parameter values obtained through curve-fitting are reported in Table 1. Considering the rate constant (*k*) values, it is evident that the fast polymerization rate allows PANI to grow in a one-dimensional morphology. The most pronounced difference between the polymerization conditions in

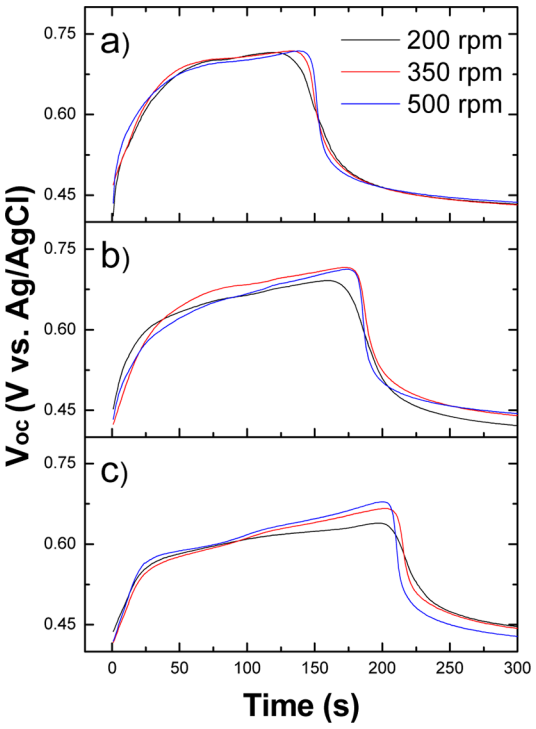

Figure 2. Open-circuit potential profiles measured during the chemical polymerization processes of PANI nanostructures at different PVP concentrations and stirring speeds: the feeding amount of PVP: (a) 0 g, (b) 2 g, and (c) 4 g.

TABLE 1. Parameters Calculated from the Kinetic Model Describing the Chemical Polymerization of Aniline in the Initial Stage

	parameters			
structure	β_1	β_2	K (V M)	k (M^{-1} s^{-1})
nanospheres	−0.24	0.07	0.16	$2.3 \times 10^{-1} \pm 0.2 \times 10^{-1}$
nanorods	−0.24	0.04	0.16	$1.4 \times 10^{-1} \pm 0.2 \times 10^{-1}$
nanofibers	−0.24	0.03	0.16	$9.2 \times 10^{-2} \pm 0.8 \times 10^{-2}$

each case was the concentration of PVP. Generally, PVP provides indirect steric effect, and it can also be directly adsorbed onto the particle surface.[44] The adsorption of PVP onto the growing particle surface makes the particle more hydrophilic, which lowers the interfacial tension between the particle and water molecules. The lowered interfacial tension is unfavorable to the generation of spherical nanostructures. Considering this, it is believed that the steric effect of PVP plays a key role in altering the polymerization kinetics.

First, Figure 3 shows the powder X-ray diffraction (XRD) patterns of PANI nanostructures. Four broad peaks centered at 2θ = 10, 16, 20, and 25° were observed in all samples, suggesting that they have partly crystalline structures. According to a previous report,[45] these characteristic peaks are consistent with those of PANI emeraldine salt in a pseudo-orthorhombic unit cell. It appeared that the nanofibers had

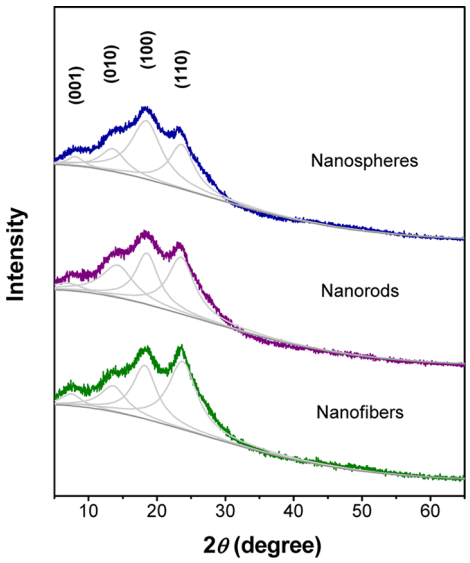

Figure 3. XRD patterns of PANI nanostructures: each XRD pattern was deconvoluted into its individual components (gray lines).

relatively high peak intensity compared to those of the other two nanostructures. The degree of crystallinity can be estimated from the area ratio of the crystalline peak to all peaks. The percentage crystallinity values of nanospheres, nanorods, and nanofibers were 30.8, 31.6, and 32.7%, respectively. It is also noteworthy that there was a gradual change in the (110) peak intensity. The nonconductive PANI emeraldine base has no observable peak at the (110) position, whereas the (110) peak gradually emerges with protonation of the imine nitrogen. In Figure 3, the (110) peak intensity increased apparently in the order of nanospheres < nanorods < nanofibers. The (110) reflection corresponds to the face-to-face interchain stacking distance (*ca.* 3.5 Å) between phenyl rings. Accordingly, the increase in the intensity of the (110) peak implies improved $\pi-\pi$ interchain stacking. These results indicate that the structural ordering in the PANI chains increases with an increase in the aspect ratio of the nanostructure. It is considered that the better structural ordering leads to enhanced charge-carrier transport through elongation of the effective conjugation length.

Ultraviolet (UV)−visible spectroscopy analysis was carried out to further investigate the oxidation levels of PANI nanostructures. As displayed in Figure 4, the UV−visible spectra of the PANI nanostructures were recorded and then decomposed into individual absorption bands by multi-Gaussian curve-fitting. First, the three absorption bands at about 350, 445, and 880 nm are attributed to the $\pi-\pi^*$ (within benzenoid segment), polaron$-\pi^*$, and $\pi-$polaron transitions, respectively, in the emeraldine salt form.[46] In addition, the two absorption bands at about 295 and 680 are ascribed to the $\pi-\pi^*$ (of the phenyl ring) and exciton

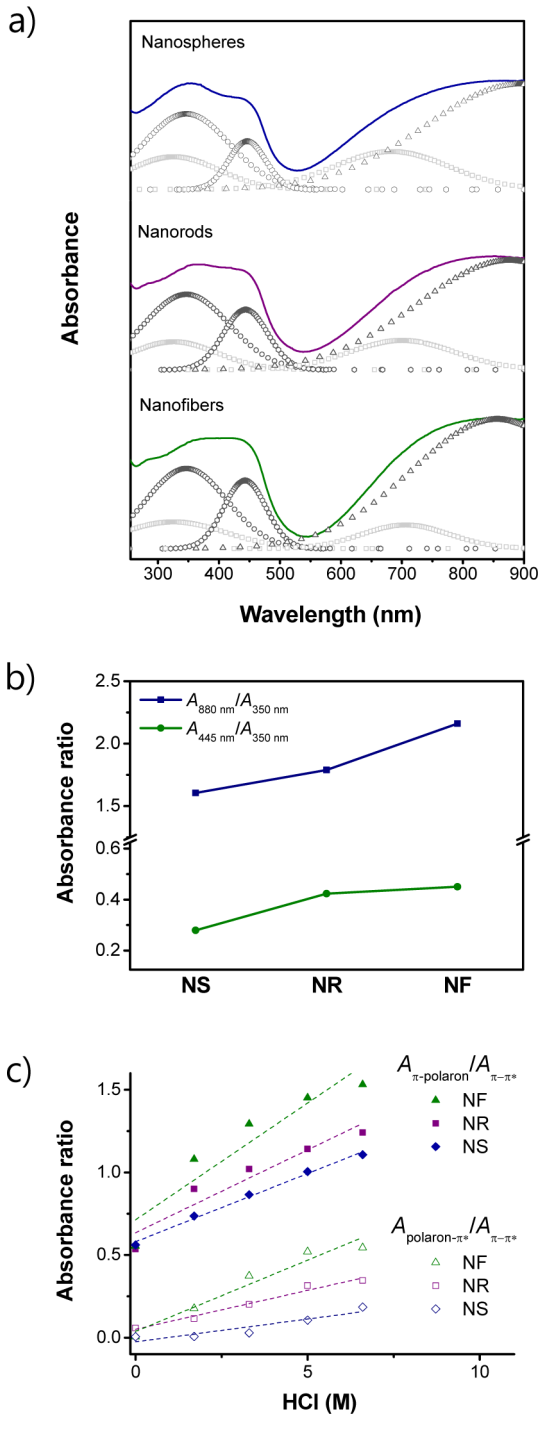

Figure 4. UV−visible spectroscopy analysis of PANI nanostructures: (a) full spectra in the range of 250−900 nm, where each spectrum (black) was deconvoluted into its individual components; (b) absorbance ratios of the 445 and 880 nm peaks relative to the 350 nm peak, which were calculated from the UV−visible spectra of PANI nanospheres (NS), nanorods (NR), and nanofibers (NF); and (c) changes in the absorbance ratios of polaron transition peak to neutral backbone peak for the PANI nanostructures upon successive exposure to hydrochloric acid.

transitions in the emeraldine base form. These results suggest that the PANI nanostructures are composed of mixed oxidation-state segments. From a qualitative

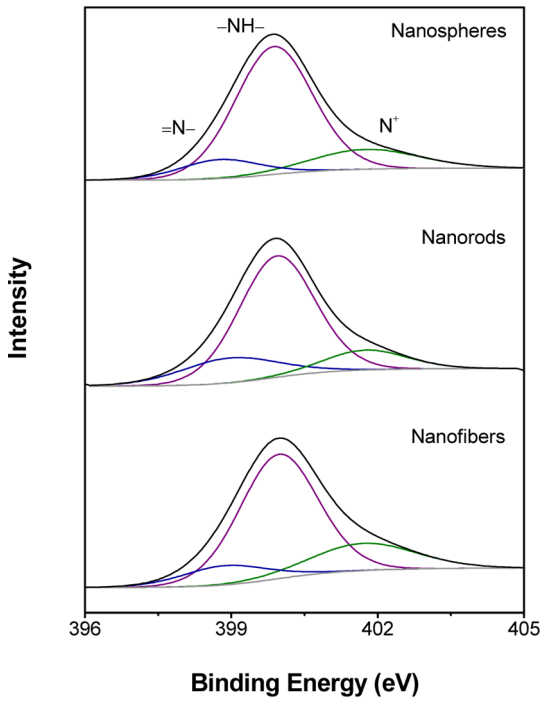

Figure 5. Representative XPS N 1s core-level spectra of PANI nanostructures.

point of view, the UV−visible spectra of the PANI nanostructures appeared to be similar to each other. However, spectral deconvolution allowed us to obtain quantitative information on the proportions of emeraldine salt relative to emeraldine base in the nanostructures. The proportions of emeraldine salt were calculated to be 65.4, 69.4, and 73.2% in nanospheres, nanorods, and nanofibers, respectively. Moreover, the absorption intensities of polaron−π^* and π−polaron transitions were found to be noticeably different between the samples. While the polaronic transitions are indicative of the emergence of charge carriers in the polymer, the $\pi-\pi^*$ transition arises from neutral benzenoid segments. Accordingly, the ratio of the absorbance of the polaronic band to that of the $\pi-\pi^*$ band provides a measure of the average oxidation level of each nanostructure. The absorbance ratios calculated from individually deconvoluted components are plotted in Figure 4b. As judged from both peak ratios of A_{445nm}/A_{350nm} and A_{880nm}/A_{350nm}, the nanofibers appear to be in the highest oxidation level. Furthermore, the PANI nanostructures were deprotonated and then gradually exposed to hydrochloric acid, during which the UV−visible spectra were recorded. The absorbance ratios of polaron transition peak to neutral benzenoid peak were plotted to estimate the rate of protonation of each nanostructure (Figure 4c). In Figure 4c, the slope is proportional to the rate of protonation of the nanostructure. The slopes were higher in the order of nanospheres < nanorods < nanofibers, indicating that the rate of protonation also follows the above trend. The aforementioned morphology-dependent crystallinity may

TABLE 2. XPS Atomic Ratios of PANI Nanostructures

	XPS atomic ratio			
structure	N^+	−NH−	=N−	$N^+/(-NH- + =N-)$
nanospheres	1.63	7.66	1.16	0.185
nanorods	1.85	7.10	1.26	0.221
nanofibers	2.23	7.66	1.27	0.250

account for the different rates of protonation of the nanostructures.

More detailed information on the oxidation state of the PANI nanostructures can be obtained through X-ray photoelectron spectroscopy (XPS) analysis. First, the binding energy peaks of carbon, nitrogen, sulfur, and oxygen were observed in the XPS spectra, indicating the presence of persulfate ions as the dopant in the PANI nanostructures. In addition, the imine nitrogen atoms of PANI are protonated in whole or in part to yield a range of oxidation states. Accordingly, the oxidation states of the PANI nanostructures can be quantitatively differentiated by scrutinizing the XPS binding energy spectra of nitrogen atoms. The typical N 1s core-level spectra of the PANI nanostructures are given in Figure 5. Each spectrum could be deconvoluted into three major components with binding energies at *ca.* 399, 400, and 402 eV, attributable to the quinonoid imine (=N−), benzenoid amine (−NH−), and positively charged nitrogen (N^+), respectively. Table 2 summarizes the atomic ratios of the related species. As the protonation level increases, the intensities of the components corresponding to the imine nitrogen atom and quinonoid imine increase, along with the decrease in the intensity of the component originating from the benzenoid amine. Higher proportions of the positively charged nitrogen and quinonoid imine were clearly found for the nanofibers, followed by the nanorods and the nanospheres. Taking all these facts into account, it is evident that the ability to transport charge carriers increases in the order of nanospheres < nanorods < nanofibers.

The intrinsic characteristics of PANI, such as doping and oxidation levels, certainly influence its electrochemical properties. In addition, the particle size and morphology can also be critical to the performance of PANI-based devices. To study the basic electrochemical properties of the three PANI samples, first, cyclic voltammetry (CV) analysis was carried out in a 1 M H_2SO_4 electrolyte. Figure 6a shows representative cyclic voltammograms of the three PANI nanostructure electrodes, in which, for comparison, the measured current has been normalized by dividing it by the weight of the PANI. The CV curves all had a similar shape, and a pair of broad redox peaks was found for each sample. In general, PANI has two redox processes, namely, the electron transfer from/to PANI (leucoemeraldine/emeraldine salt) and deprotonation/protonation (emeraldine salt/pernigraniline). The observed

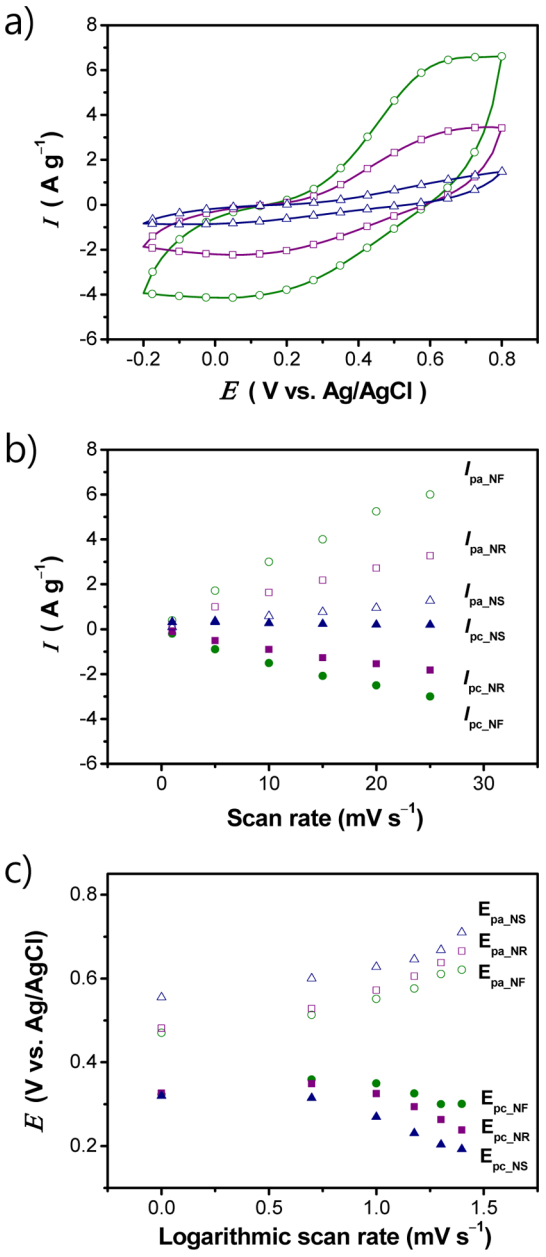

Figure 6. CV analysis of PANI nanostructures performed in a 1 M sulfuric acid solution: (a) cyclic voltammograms of electrodes consisting of PANI nanostructures at the same scan rate (25 mV s^{-1}), (b) plots of the peak current (the anodic peak current, I_{pa}; the cathodic peak current, I_{pc}) *vs* the scan rate, and (c) plots of the peak potential (the anodic peak potential, E_{pa}; the cathodic peak potential, E_{pc}) *vs* the logarithm of the scan rate.

broad redox peaks result from the overlap of the two redox processes in acidic conditions. In Figure 6a, the integrated areas of the CV curves, indicative of the capacitance of the electrode, clearly increased in the order of nanospheres < nanorods < nanofibers. Moreover, the effect of the potential scan rate on the peak current was monitored in the range of 1−25 mV s^{-1} (see Supporting Information). As seen in Figure 6b, both anodic and cathodic peak currents increased linearly with scan rate, implying that the electrode

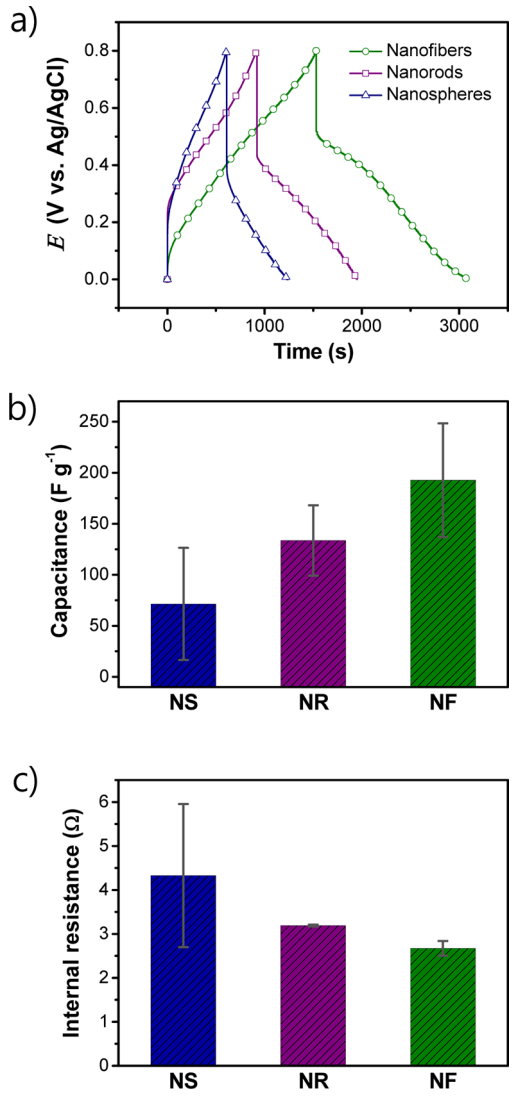

Figure 7. Capacitances of PANI nanostructure electrodes measured at a current density of 0.1 A g^{-1} in a three-electrode cell: (a) representative galvanostatic charge/discharge curves, (b) gravimetric discharge capacitances, and (c) internal resistances estimated from the *iR* drop.

kinetics are subject to a surface-controlled redox process. In other words, the redox process was found to be confined to the surface of the electrode, which is most likely due to the small dimensions of the polymeric nanostructure. The anodic (E_{pa}) and cathodic (E_{pc}) peak potentials are also plotted as a function of the logarithm of the scan rate in Figure 6c. The electron transfer coefficient (α) and the electron transfer rate constant (k_s) were obtained from Laviron theory.[47] The α values were found to be around $3.6-3.7 \times 10^{-1}$. The k_s value (4.3×10^{-1} s^{-1}) of PANI nanofibers was higher than the k_s values of the other PANI nanostructures (nanorods, 3.1×10^{-1} s^{-1}; nanospheres, 2.6×10^{-1} s^{-1}), implying that the electron transfer capability of PANI nanofibers is superior.

PANI has been extensively used as an electrode-active material in electrochemical capacitors.[48−51] The PANI nanostructures were tested first using a three-electrode

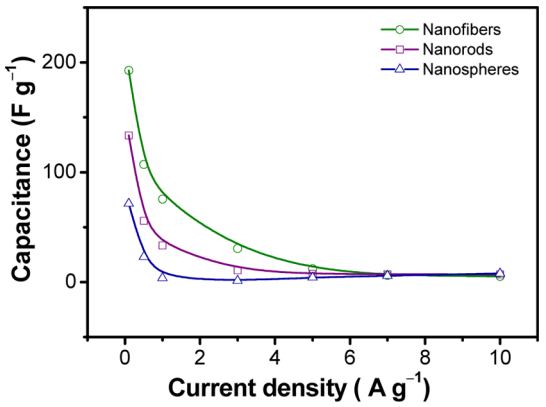

Figure 8. Comparison of specific discharge capacitances at different current densities measured in a three-electrode cell.

configuration to obtain information on their capacitances. The specific capacitance was determined from galvanostatic charge/discharge measurements, where the potential range was chosen by taking into account the CV curves. Figure 7a displays the typical galvanostatic charge/discharge profiles of the PANI nanostructure electrodes at a current density of 0.1 A g^{-1}, allowing direct comparison between the performances of individual samples. The discharging time increased in the order of nanospheres < nanorods < nanofibers over the same potential range, indicating that the nanofiber electrode has the highest specific discharge capacitance. The specific capacitances were calculated from discharge curves to be 71, 133, and 192 F g^{-1} for nanospheres, nanorods, and nanofibers, respectively (Figure 7b). In Figure 7c, the internal resistance of the nanostructure electrodes can also be estimated from the voltage drop at the beginning of each discharge curve. It was found that the internal resistance was inversely proportional to the capacitance (Figure 7c). The charge/discharge behavior was also explored at various currents densities ranging from 0.1 to 10 A g^{-1}. The variations of the discharge capacitance with current density are plotted in Figure 8. Although the specific capacitances decreased at current densities of more than 0.1 A g^{-1}, the above tendency of the capacitance value remained unchanged over the entire current density range. It is well-known that the surface area of electrode materials highly affects the performance of capacitors. In addition, it is believed that the performance of conducting polymer capacitors depends on the oxidation level of the polymer. To clarify which factors are responsible for the capacitor performance, the areal capacitance was also calculated by dividing the gravimetric capacitance by the BET surface area of the nanostructure (see Supporting Information). The areal capacitances also increased in the order of nanospheres (19×10^{-1} F m^{-2}) < nanorods (27×10^{-1} F m^{-2}) < nanofibers (38×10^{-1} F m^{-2}), confirming that the oxidation level of the PANI nanostructures was one of the crucial factors for determining the capacitor performance.

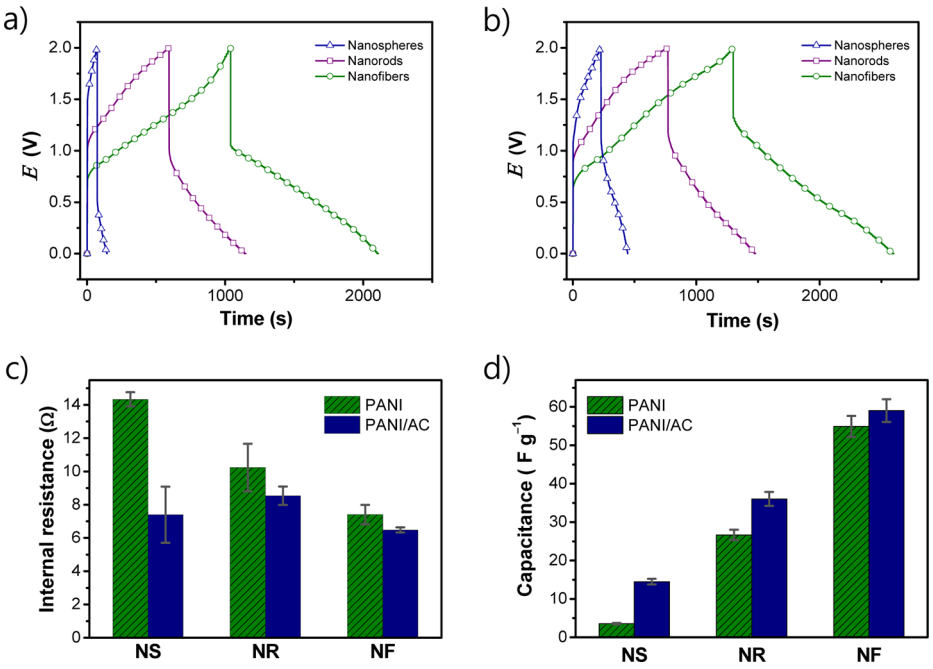

Figure 9. Capacitances of PANI nanostructure electrodes measured at a current density of 0.1 A g^{-1} in a stainless steel capacitor cell: (a) representative galvanostatic charge/discharge curves. Effect of conductive additive on the capacitance: (b) galvanostatic charge/discharge curves of activated carbon/PANI nanostructure electrodes, (c,d) comparison of (c) internal resistances and (d) discharge capacitances.

The performance of the PANI electrodes was also evaluated in a real capacitor cell. The PANI nanoparticles were pressed into pellets (10 mm in diameter and 0.7 mm in thickness) without any additives and then assembled into the test cell. Galvanostatic charge/discharge curves were obtained for individual samples at a cell voltage range of 2 V (Figure 9a). The discharge capacitances were calculated to be 4, 27, and 55 F g^{-1} for nanospheres, nanorods, and nanofibers, respectively. Although the high resistance of the stainless steel cell would lead to a decrease in capacitance value, the trend is commensurate with the results obtained in the three-electrode configuration. Therefore, it is reasonably concluded that the intrinsic properties of the PANI nanostructures primarily account for the capacitor performance. Besides, the capacitor electrode is composed of numerous nanoparticles, and thus the capacitor performance can also be subject to how the nanoparticles are assembled in the electrode. It is expected that there would be considerable contact resistance between the nanoparticles forming the electrodes. The interparticle contact resistance could make up a great part of the internal resistance of the electrode. In order to control the interparticle contact resistance, activated carbon powder as a conductive agent was added into the PANI nanostructure electrodes. Figure 9b shows the galvanostatic charge/discharge curves of activated carbon/PANI nanostructure electrodes. The internal resistances of all samples were reduced by adding the activated carbon powder (Figure 9c). In particular, PANI nanosphere electrodes showed a 50% decrease in their internal resistance. The internal resistance can be mitigated by improving structural and electrical contact between PANI nanostructures with the aid of the carbon additive. Structurally, the lower the aspect ratio of the nanostructures, the higher the interparticle contact resistance.[52] It is therefore considered that the carbon additive exerts a more positive influence on low aspect ratio nanostructures in terms of reducing the contact resistance. The discharge capacitances of PANI nanosphere, nanorod, and nanofiber electrodes also increased 4.0-, 1.4-, and 1.1-fold after addition of the carbon additive (Figure 9d). Because the amounts of the carbon additive added were the same, the surface areas of the electrodes would equivalently increase. Accordingly, it can be interpreted that the decreased internal resistance directly accounts for the change in capacitance. The capacitance also showed higher rates of increase with decreasing aspect ratio of the nanostructures, which is consistent with the case of the internal resistance.

CONCLUSIONS

The use of a steric stabilizer allowed kinetic control of the anisotropic growth of PANI during chemical polymerization, making it possible to fabricate three different nanostructures, namely, nanospheres, nanorods, and nanofibers. These nanostructures with different aspect ratios offered a good opportunity to study the dependence of their main properties on the morphology. Interestingly, the oxidation/protonation level and crystallinity of the nanostructures increased with

increasing aspect ratio. The electron transfer capability of the nanostructures was also found to increase in the order of nanospheres < nanorods < nanofibers. Furthermore, the capacitors based on the nanostructures showed morphology-dependent capacitance values, where the interparticle contact resistance was identified as a critical parameter. It is expected that the above findings may provide a new insight into tailoring nanostructures as well as an essential understanding of the parameters determining device performance.

MATERIALS AND METHODS

Materials. Aniline and APS were purchased from Sigma-Aldrich, and 37% hydrochloric acid (HCl) solution was obtained from Merck. The solubility of aniline in water is 3.6 g mL^{-1} at 20 °C. PVP (M_w = 10 000, Sigma-Aldrich) was employed as a stabilizer. Poly(vinylidene fluoride) (PVDF; KF1300 binder, Kureha) was used as a binder to construct the electrode. *N*-Methylpyrrolidinone (NMP; Sigma-Aldrich) was employed as a solvent for dissolving the PVDF. Activated carbon powder was used as a conductive filler. Distilled water was used for all polymerization experiments.

Synthesis of PANI Nanostructures. PANI nanostructures were fabricated with different stabilizer concentrations in aqueous solution. The main synthetic conditions are listed in Table S1 in the Supporting Information. Aniline was first dissolved in aqueous HCl solution (70 mL), and then PVP was added to the solution. Chemical oxidation polymerization of aniline was initiated by adding APS into the above solution. All reaction steps were carried out under magnetic stirring at 25 °C. The polymerization proceeded for 2 h, and then the resulting deep green product was washed with excess ethanol and water to remove impurities such as residual monomers, stabilizer, and oxidizing agent. The desired product was finally retrieved by centrifugation and allowed to dry in a vacuum oven at 25 °C.

Characterization. SEM was carried out using a JEOL JSM-7500F microscope to observe the morphology of the nanomaterials. The specimens were coated with a thin layer of gold to eliminate charging effects. The dimensions of the nanostructures were extracted from the SEM images using I-solution lite (IMT i-solution inc.) software. XRD measurements were performed using an X'Pert PRO multipurpose X-ray diffractometer equipped with a Cu Kα radiation source (λ = 1.5406 Å). Lorentzian fitting was used to gain information on the areas of peaks and their full width at half-maxima. UV−visible spectra were taken from diluted PANI/ethanol dispersions using a JASCO V-550 spectrophotometer. Multipeak fitting was carried out by using Gaussian functions, and the absorbance ratios were calculated by using the integrated area values of individual components. For the deprotonation, the samples were treated with 0.1 N $NaOH_4$ and then washed with excess water. XPS was performed using a Thermo VG Scientific Multilab 2000 spectrometer with an Mg/Al twin-anode excitation source. The specimens were pelletized and then mounted on the standard sample studs by means of double-sided adhesive tape. Peak fitting of the collected spectra was conducted with VG Avantage software supplied by the manufacturer. BET surface areas were calculated through nitrogen sorption experiments using a Micromeritics ASAP2020 instrument.

Electrochemical Measurements. Open-circuit potential was measured as a function of time using a two-electrode cell, where the working and reference electrodes were Pt and Ag/AgCl, respectively. The potential was recorded throughout the course of the polymerization by using a Wonatech WMPG 1000 potentiostat/galvanostat. CV and galvanostatic charge/discharge experiments were performed in a three-electrode cell containing 1 M H_2SO_4 solution using a Pt auxiliary electrode and a Ag/AgCl reference electrode. Mixtures of PANI nanostructures (97.5 wt %) and PVDF (2.5 wt %) dissolved in NMP were coated onto stainless steel wires, which were employed as working electrodes after drying in vacuum at 30 °C. A two-electrode capacitor cell was built with a polypropylene separator and stainless steel current collectors using a symmetrical construction. In this case, PANI nanostructures were pressed into pellets without any additional binder, and the same acid solution, 1 M H_2SO_4, was employed as an electrolyte. When a conductive agent was used to examine the effect of interparticle resistance, PANI nanostructures were mixed with activated carbon (10 wt %) and then pressed. The specific capacitance was calculated from the discharge curves of galvanostatic cycles, according to $C = I/(dE/dt)$, where I is the constant discharge current density, E is the cell voltage, and dE/dt is the slope of the discharge curve.

Conflict of Interest: The authors declare no competing financial interest.

Acknowledgment. This research was financially supported by Chonnam National University, 2011, and the International S&T Cooperation Program (K20901002259-12E0100-01510) through the National Research Foundation of Korea funded by the Ministry of Education, Science and Technology.

Supporting Information Available: (1) Detailed synthetic conditions; (2) SEM images obtained at different stirring speeds; (3) UV-visible spectra upon successive exposure to hydrochloric acid; (4) discharge capacitances measured at different current densities; (5) cyclic voltammograms measured at different scan rates; (6) areal capacitances. This material is available free of charge *via* the Internet at http://pubs.acs.org.

REFERENCES AND NOTES

1. Jang, J. Conducting Polymer Nanomaterials and Their Applications. *Adv. Polym. Sci.* **2006**, *199*, 189–259.
2. Li, Y. F. Conducting Polymers. *Prog. Chem.* **2002**, *14*, 207–211.
3. Gerard, M.; Chaubey, A.; Malhotra, B. D. Application of Conducting Polymers to Biosensors. *Biosens. Bioelectron.* **2002**, *17*, 345–359.
4. Mastragostino, M.; Arbizzani, C.; Soavi, F. Conducting Polymers as Electrode Materials in Supercapacitors. *Solid State Ionics* **2002**, *148*, 493–498.
5. Aradilla, D.; Estrany, F.; Aleman, C. Symmetric Supercapacitors Based on Multilayers of Conducting Polymers. *J. Phys. Chem. C* **2011**, *115*, 8430–8438.
6. Kim, B. C.; Too, C. O.; Kwon, J. S.; Bo, J. M.; Wallace, G. G. A Flexible Capacitor Based on Conducting Polymer Electrodes. *Synth. Met.* **2011**, *161*, 1130–1132.
7. Liu, D. Y.; Reynolds, J. R. Dioxythiophene-Based Polymer Electrodes for Supercapacitor Modules. *ACS Appl. Mater. Interfaces* **2010**, *2*, 3586–3593.
8. Yoon, H.; Jang, J. Conducting-Polymer Nanomaterials for High-Performance Sensor Applications: Issues and Challenges. *Adv. Funct. Mater.* **2009**, *19*, 1567–1576.
9. Mulchandani, A.; Myung, N. V. Conducting Polymer Nanowires-Based Label-Free Biosensors. *Curr. Opin. Biotechnol.* **2011**, *22*, 502–508.
10. Yoon, H.; Lee, S. H.; Kwon, O. S.; Song, H. S.; Oh, E. H.; Park, T. H.; Jang, J. Polypyrrole Nanotubes Conjugated with Human Olfactory Receptors: High-Performance Transducers for FET-Type Bioelectronic Noses. *Angew. Chem., Int. Ed.* **2009**, *48*, 2755–2758.
11. Xu, J. J.; Wang, K.; Zu, S. Z.; Han, B. H.; Wei, Z. X. Hierarchical Nanocomposites of Polyaniline Nanowire Arrays on Graphene Oxide Sheets with Synergistic Effect for Energy Storage. *ACS Nano* **2010**, *4*, 5019–5026.
12. Al-Mashat, L.; Shin, K.; Kalantar-Zadeh, K.; Plessis, J. D.; Han, S. H.; Kojima, R. W.; Kaner, R. B.; Li, D.; Gou, X. L.; Ippolito, S. J.; Wlodarski, W. Graphene/Polyaniline Nanocomposite for Hydrogen Sensing. *J. Phys. Chem. C* **2010**, *114*, 16168–16173.
13. Alvi, F.; Ram, M. K.; Basnayaka, P. A.; Stefanakos, E.; Goswami, Y.; Kumar, A. Graphene-Polyethylenedioxythiophene

Conducting Polymer Nanocomposite Based Supercapacitor. *Electrochim. Acta* **2011**, *56*, 9406–9412.
14. Bangar, M. A.; Shirale, D. J.; Purohit, H. J.; Chen, W.; Myung, N. V.; Mulchandani, A. Single Conducting Polymer Nanowire Based Sequence-Specific, Base-Pair-Length Dependant Label-Free DNA Sensor. *Electroanalysis* **2011**, *23*, 371–379.
15. Yoon, H. S.; Choi, M. J.; Lee, K. A.; Jang, J. S. Versatile Strategies for Fabricating Polymer Nanomaterials with Controlled Size and Morphology. *Macromol. Res.* **2008**, *16*, 85–102.
16. Li, D.; Huang, J. X.; Kaner, R. B. Polyaniline Nanofibers: A Unique Polymer Nanostructure for Versatile Applications. *Acc. Chem. Res.* **2009**, *42*, 135–145.
17. Wang, D. W.; Li, F.; Zhao, J. P.; Ren, W. C.; Chen, Z. G.; Tan, J.; Wu, Z. S.; Gentle, I.; Lu, G. Q.; Cheng, H. M. Fabrication of Graphene/Polyaniline Composite Paper *via In Situ* Anodic Electropolymerization for High-Performance Flexible Electrode. *ACS Nano* **2009**, *3*, 1745–1752.
18. Huang, J. X.; Kaner, R. B. The Intrinsic Nanofibrillar Morphology of Polyaniline. *Chem. Commun.* **2006**, 367–376.
19. Chiou, N. R.; Epstein, A. J. Polyaniline Nanofibers Prepared by Dilute Polymerization. *Adv. Mater.* **2005**, *17*, 1679.
20. Zhang, X. Y.; Kolla, H. S.; Wang, X. H.; Raja, K.; Manohar, S. K. Fibrillar Growth in Polyaniline. *Adv. Funct. Mater.* **2006**, *16*, 1145–1152.
21. Rahy, A.; Sakrout, M.; Manohar, S.; Cho, S. J.; Ferraris, J.; Yang, D. J. Polyaniline Nanofiber Synthesis by Co-Use of Ammonium Peroxydisulfate and Sodium Hypochlorite. *Chem. Mater.* **2008**, *20*, 4808–4814.
22. Rahy, A.; Rguig, T.; Cho, S. J.; Bunker, C. E.; Yang, D. J. Polar Solvent Soluble and Hydrogen Absorbing Polyaniline Nanofibers. *Synth. Met.* **2011**, *161*, 280–284.
23. Surwade, S. P.; Agnihotra, S. R.; Dua, V.; Manohar, N.; Jain, S.; Ammu, S.; Manohar, S. K. Catalyst-Free Synthesis of Oligoanilines and Polyaniline Nanofibers Using H_2O_2. *J. Am. Chem. Soc.* **2009**, *131*, 12528.
24. Ding, H. J.; Wan, M. X.; Wei, Y. Controlling the Diameter of Polyaniline Nanofibers by Adjusting the Oxidant Redox Potential. *Adv. Mater.* **2007**, *19*, 465.
25. Lin, Y. F.; Chen, C. H.; Xie, W. J.; Yang, S. H.; Hsu, C. S.; Lin, M. T.; Jian, W. B. Nano Approach Investigation of the Conduction Mechanism in Polyaniline Nanofibers. *ACS Nano* **2011**, *5*, 1541–1548.
26. Wang, W.; Li, Z. Y.; Xu, X. R.; Dong, B.; Zhang, H. N.; Wang, Z. J.; Wang, C.; Baughman, R. H.; Fang, S. L. Au-Doped Polyacrylonitrile-Polyaniline Core−Shell Electrospun Nanofibers Having High Field-Effect Mobilities. *Small* **2011**, *7*, 597–600.
27. Han, J.; Li, L. Y.; Guo, R. Novel Approach to Controllable Synthesis of Gold Nanoparticles Supported on Polyaniline Nanofibers. *Macromolecules* **2010**, *43*, 10636–10644.
28. Liao, Y. Z.; Zhang, C.; Wang, X.; Li, X. G.; Ippolito, S. J.; Kalantar-Zadeh, K.; Kaner, R. B. Carrier Mobility of Single-Walled Carbon Nanotube-Reinforced Polyaniline Nanofibers. *J. Phys. Chem. C* **2011**, *115*, 16187–16192.
29. Liang, Y.; Gu, L.; Liu, X. Q.; Yang, Q. Y.; Kajiura, H.; Li, Y. M.; Zhou, T. S.; Shi, G. Y. Composites of Polyaniline Nanofibers and Molecularly Imprinted Polymers for Recognition of Nitroaromatic Compounds. *Chem.—Eur. J.* **2011**, *17*, 5989–5997.
30. Baker, C. O.; Shedd, B.; Innis, P. C.; Whitten, P. G.; Spinks, G. M.; Wallace, G. G.; Kaner, R. B. Monolithic Actuators from Flash-Welded Polyaniline Nanofibers. *Adv. Mater.* **2008**, *20*, 155.
31. Huang, J.; Virji, S.; Weiller, B. H.; Kaner, R. B. Nanostructured Polyaniline Sensors. *Chem.—Eur. J.* **2004**, *10*, 1315–1319.
32. Liao, Y. Z.; Zhang, C.; Zhang, Y.; Strong, V.; Tang, J. S.; Li, X. G.; Kalantar-zadeh, K.; Hoek, E. M. V.; Wang, K. L.; Kaner, R. B. Carbon Nanotube/Polyaniline Composite Nanofibers: Facile Synthesis and Chemosensors. *Nano Lett.* **2011**, *11*, 954–959.
33. Fowler, J. D.; Virji, S.; Kaner, R. B.; Weiller, B. H. Hydrogen Detection by Polyaniline Nanofibers on Gold and Platinum Electrodes. *J. Phys. Chem. C* **2009**, *113*, 6444–6449.
34. Zhao, M.; Wu, X. M.; Cai, C. X. Polyaniline Nanofibers: Synthesis, Characterization, and Application to Direct Electron Transfer of Glucose Oxidase. *J. Phys. Chem. C* **2009**, *113*, 4987–4996.
35. Baker, C. O.; Shedd, B.; Tseng, R. J.; Martinez-Morales, A. A.; Ozkan, C. S.; Ozkan, M.; Yang, Y.; Kanert, R. B. Size Control of Gold Nanoparticles Grown on Polyaniline Nanofibers for Bistable Memory Devices. *ACS Nano* **2011**, *5*, 3469–3474.
36. Tseng, R. J.; Huang, J. X.; Ouyang, J.; Kaner, R. B.; Yang, Y. Polyaniline Nanofiber/Gold Nanoparticle Nonvolatile Memory. *Nano Lett.* **2005**, *5*, 1077–1080.
37. Wang, J.; Qi, X.; Meng, F.; Ning, Y.; Chen, S. F.; Pang, D.; Wen, Y. F. Polyaniline Nanofibers: Inducing Action of Neodymium Oxide and Inhibiting Effect on Electrochemical Degradation and Modified Platinum Electrode Application to the Electrocatalytic Oxidation of Methanol. *J. Phys. Chem. C* **2009**, *113*, 1459–1465.
38. Hyder, M. N.; Lee, S. W.; Cebeci, F. C.; Schmidt, D. J.; Shao-Horn, Y.; Hammond, P. T. Layer-by-Layer Assembled Polyaniline Nanofiber/Multiwall Carbon Nanotube Thin Film Electrodes for High-Power and High-Energy Storage Applications. *ACS Nano* **2011**, *5*, 8552–8561.
39. Guan, H.; Fan, L. Z.; Zhang, H. C.; Qu, X. H. Polyaniline Nanofibers Obtained by Interfacial Polymerization for High-Rate Supercapacitors. *Electrochim. Acta* **2010**, *56*, 964–968.
40. Cao, Y.; Mallouk, T. E. Morphology of Template-Grown Polyaniline Nanowires and Its Effect on the Electrochemical Capacitance of Nanowire Arrays. *Chem. Mater.* **2008**, *20*, 5260–5265.
41. Ghenaatian, H. R.; Mousavi, M. F.; Rahmanifar, M. S. High Performance Battery-Supercapacitor Hybrid Energy Storage System Based on Self-Doped Polyaniline Nanofibers. *Synth. Met.* **2011**, *161*, 2017–2023.
42. Li, D.; Kaner, R. B. Shape and Aggregation Control of Nanoparticles: Not Shaken, Not Stirred. *J. Am. Chem. Soc.* **2006**, *128*, 968–975.
43. Gill, M. T.; Chapman, S. E.; DeArmitt, C. L.; Baines, F. L.; Dadswell, C. M.; Stamper, J. G.; Lawless, G. A.; Billingham, N. C.; Armes, S. P. A Study of the Kinetics of Polymerization of Aniline Using Proton NMR Spectroscopy. *Synth. Met.* **1998**, *93*, 227–233.
44. Stejskal, J.; Kratochvil, P. Polyaniline Dispersions. 5. Poly(vinyl alcohol) and Poly(*N*-vinylpyrrolidone) as Steric Stabilizers. *Langmuir* **1996**, *12*, 3389–3392.
45. Pouget, J. P.; Józefowicz, M. E.; Epstein, A. J.; Tang, X. X-ray Structure of Polyaniline. *Macromolecules* **1991**, *24*, 779–789.
46. Feng, X. M.; Yang, G.; Xu, Q.; Hou, W. H.; Zhu, J. P. Self-Assembly of Polyaniline/Au Composites: From Nanotubes to Nanofibers. *Macromol. Rapid Commun.* **2006**, *27*, 31–36.
47. Laviron, E. General Expression of the Linear Potential Sweep Voltammogram in the Case of Diffusionless Electrochemical Systems. *J. Electroanal. Chem.* **1979**, *101*, 19–28.
48. Murugan, A. V.; Muraliganth, T.; Manthiram, A. Rapid, Facile Microwave-Solvothermal Synthesis of Graphene Nanosheets and Their Polyaniline Nanocomposites for Energy Storage. *Chem. Mater.* **2010**, *22*, 2692–2692.
49. Wu, Q.; Xu, Y. X.; Yao, Z. Y.; Liu, A. R.; Shi, G. Q. Supercapacitors Based on Flexible Graphene/Polyaniline Nanofiber Composite Films. *ACS Nano* **2010**, *4*, 1963–1970.
50. Wang, H. L.; Hao, Q. L.; Yang, X. J.; Lu, L. D.; Wang, X. A Nanostructured Graphene/Polyaniline Hybrid Material for Supercapacitors. *Nanoscale* **2010**, *2*, 2164–2170.
51. Zhang, K.; Zhang, L. L.; Zhao, X. S.; Wu, J. S. Graphene/Polyaniline Nanofiber Composites as Supercapacitor Electrodes. *Chem. Mater.* **2010**, *22*, 1392–1401.
52. Yoon, H.; Hong, J. Y.; Jang, J. Charge-Transport Behavior in Shape-Controlled Poly(3,4-ethylenedioxythiophene) Nanomaterials: Intrinsic and Extrinsic factors. *Small* **2007**, *3*, 1774–1783.